Comprehensive Characterization of a Mesoporous Cerium Oxide Nanomaterial with High Surface Area and High Thermal Stability

Elifkübra Özkan, Alexander Hofmann, Martin Votsmeier, Wu Wang, Xiaohui Huang, Christian Kübel, Felix Badaczewski, Kevin Turke, Sebastian Werner, and Bernd M. Smarsly*

ABSTRACT: In the present study, the pore space of a mesoporous cerium oxide material is investigated, which forms by the self assembly of primary particles into a spherical secondary structure possessing a disordered mesopore space. The material under study exhibits quite stable mesoporosity upon aging at high temperatures (800 °C) and is, thus, of potential interest in high temperature catalysis. Here, different characterization techniques were applied to elucidate the structural evolution taking place between heat treatment at 400 °C and aging at 800 °C, i.e., in a water containing atmosphere, which is usually detrimental to nanoscaled porosity. The changes in the mesoporosity were monitored by advanced physisorption experiments, including hysteresis scanning, and electron tomography analysis coupled with a 3D reconstruction of the mesopore space. These methods indicate that the 3D spatial arrangement of the primary particles during the synthesis under hydrothermal conditions via thermal hydrolysis is related to the thermal stability of the hierarchical mesopore structure. The assembly of the primary CeO_2 particles (~4 nm in size) results in an interparticulate space constituting an open 3D mesopore network, as revealed by skeleton analysis of tomography data, being in conformity with hysteresis scanning. At elevated temperatures (800 °C), sinter processes occur resulting in the growth of the primary particles, but the 3D mesopore network and the spherical secondary structure are preserved.

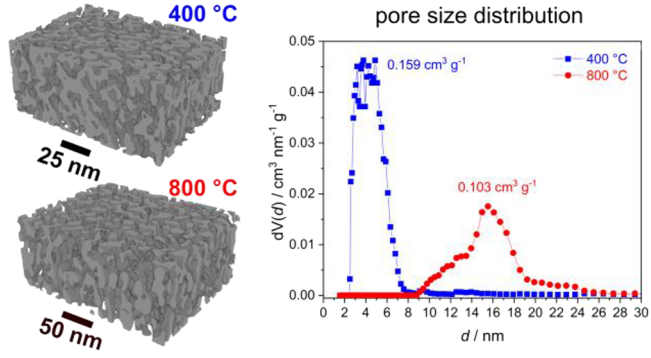

INTRODUCTION

Cerium oxide is a widely investigated nanomaterial, which attracts great interest in technological applications because of the ability of cerium to shuttle between Ce^{3+} and Ce^{4+} states. This unique redox chemistry is the origin of the high oxygen storage capacity making it a promising oxidation catalyst material.[1] Hence, CeO_2 based materials with nanoscaled porosity are already applied as promoters in heterogeneous catalytic processes like in three way catalysts (TWCs) for the elimination of toxic exhaust gases from automobiles.[2] Furthermore, CeO_2 nanomaterials are studied as catalysts for other economically relevant oxidation and reduction reactions like the HCl oxidation, CO oxidation, and NO reduction.[1−4] Many wet chemical approaches have been developed for the synthesis of CeO_2 nanomaterials allowing for the manipulation of characteristics like size and shape.[5,6] Among them, the mesoporous nanomaterials are characterized by a high surface area, which is an essential requirement for high catalytic activity enhancing the contact between the catalyst and the reactants. The synthesis of mesoporous CeO_2 is carried out, for example, by nanocasting utilizing hard templates, such as SBA-15 and KIT 6 silica,[7,8] or by the self assembly of preformed CeO_2 nanoparticles into a highly ordered 3D mesostructure by the assistance of polymers.[9−11] Another example for the preparation of a CeO_2 nanomaterial equipped with a high surface area is the thermal hydrolysis of a cerium precursor at elevated temperatures (120−240 °C).[12,13] It is based on the control of the agglomeration of the primary particles to a spherical secondary structure leading to a disordered mesoporous nanomaterial with pronounced stability against thermal treatment and aging at 800 °C.

In addition to the surface area, the nanonmaterial's performance can be tuned by tailoring the particle morphology by suitable synthetic concepts.[14] Furthermore, high temperatures can occur during the catalytic reactions, leading to sinter effects beyond 600 °C and therefore to a loss of surface area. Hence, thermal stability of the nanostructure is mandatory for maintaining high catalytic activity under working conditions.

Consequently, a general understanding of the impact of thermal treatment and sintering on the pore space is of prime interest.

In the present study, a mesoporous CeO_2 synthesized by thermal hydrolysis is used as a case study to elucidate the transformation of a disordered mesopore space upon thermally induced crystallization and sintering. This previously introduced CeO_2 material forms by the self assembly of primary nano particles into a secondary structure, spherical particles, on the micrometer scale, which are preserved even upon aging at 800 °C, i.e., in a water containing atmosphere, which is usually quite detrimental to nanoscaled porosity in metal oxides.[12,13] In our previous study, we had investigated the formation of the primary particles during the thermal hydrolysis of an aqueous solution of $(NH_4)_2Ce(NO_3)_6$ (briefly CAN) at temperatures between room temperature and 100 °C by a thorough in situ SAXS analysis. We had proposed that they assemble to the observed spherical superstructure during the hydrothermal treatment of the reaction solution (Scheme 1).[15] In detail, this recent study

Scheme 1. Proposed Mechanism for the Thermal Hydrolysis with the Formation of the Primary Particles and Their Agglomeration to nm sized Species at T = 25−100 °C and Their Self Assembly into the μm sized Secondary Structure

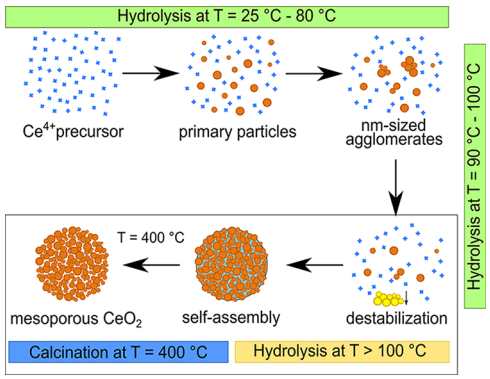

has revealed that the formed 2 nm primary particles possess a high tendency for agglomeration into 5−20 nm particles upon the hydrolysis above 60 °C. Consequently, the nanobuilding blocks for the superstructure are the primary particles and also their nanometer sized agglomerates (Scheme 1). Based on these results, the objective of the present study is to investigate their mutual assembly and arrangement into the stable secondary structure and the resulting mesoporosity after the calcination at 400 °C and hydrothermal aging at 800 °C (marked in a box in Scheme 1).

Here, the structural changes in the mesopore space occurring at elevated temperatures due to sintering effects are correlated to the chemical transformation of the material, evidenced by thermogravimetric analysis coupled with mass spectrometry (TG MS). To characterize the pore space, state of the art small angle scattering, physisorption, and electron tomography analyses were applied, which provide complementary informa tion about the disordered nanomaterial. Small angle X ray scattering (SAXS), X ray diffraction (XRD), and standard physisorption analysis were used to determine parameters characterizing the mesopore space like the particle dimension, pore size, pore shape, pore connectivity, and porosity. In particular, here, we apply the physisorption hysteresis scanning method using argon, which is a state of the art technique to elucidate the connectivity in mesoporous frameworks. In such experiments, in subsequent cycles partial isotherms are measured within the relative pressure range in which hysteresis occurs and deliver information about the evaporation mechanism in the pores (i.e., capillary evaporation or pore blocking/cavitation), which is directly correlated to the pore network and geometry.[16−18] SAXS analysis was performed taking advantage of the concept of the "chord length distribution" (CLD) to describe the disordered mesopore space, the parameters being related to physisorption and electron tomography. However, such bulk characterization techniques yield averaged results and ignore topological properties. On the other hand, scanning electron microscopy (SEM) and transmission electron microscopy (TEM) provide local structural and morphological information.

Thus, electron tomography was applied to elucidate the complex 3D structure of the mesoporosity for different heat treatment temperatures.[19] After acquisition of a series of 2D images at different projection directions in TEM, these projections are combined to reconstruct a 3D representation of the investigated material.[20,21] This technique was recently extensively used for the characterization of the porosity of macro and mesoporous silica monoliths[22−24] and mesoporous carbons.[25]

Hence, in contrast to these previous studies, in the present work, a material is investigated, which is mesoporous and nanocrystalline at the same time. Thus, the crystallinity of the constituting oxide has an important difference to the previous in depth studies, mainly addressing amorphous porous SiO_2 materials, especially with respect to the impact of temperature treatment at elevated temperature under reaction conditions.

In essence, our study presents a conceptual methodology to elucidate the alterations in the disordered mesopore space in relation to the growth of the CeO_2 nanocrystals and the parallel chemical alterations, combining XRD, nitrogen physisorption measurements with TG MS, and Raman spectroscopy. The TG MS analysis delivers insights into the chemical changes at elevated temperatures and, thus, provides guidance to the structural evolution occurring due to the removal of species such as H_2O, NO_3^-, etc., on the particle surface. This comprehensive approach finally provides relevant insights into the factors affecting the stability of the mesopore space even under harsh conditions resembling the environment in catalytic reactions. Thereby, this study introduces a methodology to understand the pronounced stability of the mesoporosity of a CeO_2 material synthesized by thermal hydrolysis and thus provides guidelines for the rational design of crystalline nanoscaled materials with advanced thermal stability of the mesopore space.

EXPERIMENTAL SECTION

Preparation of the Mesoporous CeO_2. The fabrication of mesoporous CeO_2 was adapted from the synthesis by Ohtake et al.[12] and by Hirano et al.[13] and is based on the thermal hydrolysis method. An aqueous solution of CAN was prepared with a concentration of 20 g/L in terms of CeO_2 and heated at 150 °C for 3 h. After the hydrothermal treatment, aqueous ammonia was added to the reaction solution until pH = 8. The obtained precipitate was filtered and dried at 80 °C overnight. After that, the CeO_2 powder was calcined at 400 °C for 10 h (hereinafter named fresh) and aged at 800 °C for 16 h in a 10% water atmosphere (hereinafter named aged).

Characterization of the CeO_2 Powder. The crystallinity of the powder was studied by XRD analysis, which was performed with an X'Pert Pro diffractometer from Panalytical Instruments using Cu Kα radiation with an acceleration voltage of 40 kV and an emission current

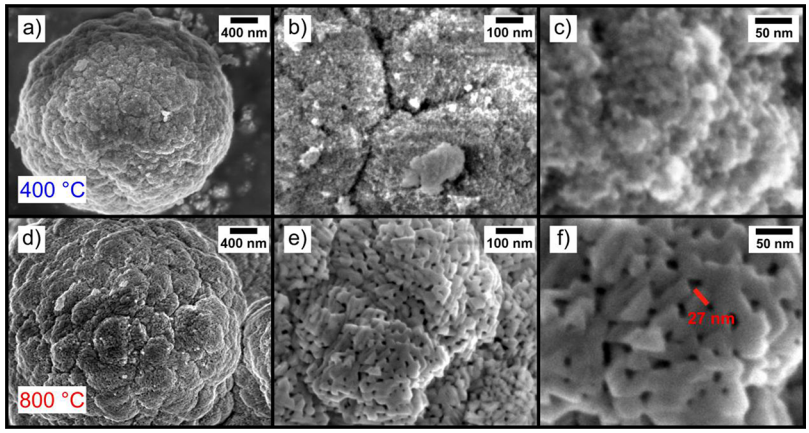

Figure 1. SEM images of the powders after calcination at 400 °C (a–c) and after aging at 800 °C (d–f). In (f), the mesopores can be seen being present even after harsh aging.

of 40 mA. The crystallite size was determined by applying the Scherrer equation.

The SAXS experiments have been performed at Beamline 5.2 (SAXS) in the Elettra Synchrochron Facility (Trieste, Italy) with a radiation energy of 8 keV. The data were recorded using a Pilatus3 1M.

TG analysis was performed on a STA 409PC thermoscale (Netzsch) in combination with a QMG421 quadrupole mass spectrometer (MS) from Balzers with an ionization energy of 70 eV. A temperature range between 25 and 1000 °C was analyzed with a heating rate of of 5 °C/min in synthetic air (80% N_2, 20% O_2).

Raman spectroscopy was performed using a Senterra Raman spectrometer (Bruker) with OPUS 7.5 software. A Nd:YAG laser (λ = 532 nm) with a laser power of 0.2 mW was used. Measurements were conducted with a spectral resolution of 3–5 cm^{-1}, coaddition of 50 scans, and 3 s integration time.

The morphology of the mesoporous CeO_2 was examined via SEM carried out on a Zeiss Merlin instrument with an acceleration voltage of 3 kV and a current of 100 pA. In order to increase the conductivity of the samples, the films were coated with 2 nm carbon film. Further morphological characterization of the powder was carried out by TEM using a Philips CM30 instrument equipped with a LaB_6 cathode (300 kV). The samples were suspended in ethanol and drop cast on carbon sputtered copper grids (Plano). After drying, the grids were loaded.

For insight into the mesopore structure nitrogen physisorption experiments were performed at 77 K with an automated gas adsorption station Quadrasorb EVO by Quantachrome Instruments. The argon physisorption measurements as well as the hysteresis scanning experiments were conducted with an automated gas adsorption station Autosorb iQ2 by Quantachrome Instruments at 87 K by using a cryostat (CryoSync). Prior to the measurements, the samples were degassed in vacuum for 12 h at 120 °C. The surface area was determined using the BET method, and the pore size distributions were calculated via the nonlocal density functional theory (NLDFT) approach, using the adsorption branch of the isotherm unless it is explicitly mentioned that the desorption branch is used. Cylindrical pore kernels were assumed for the system silica/nitrogen (77 K) and for argon on zeolites/silica (87 K). A moving point average of 5 was applied to the pore size distributions.

For the tomography analysis,[21] a small amount (~10 mg) of the fresh and aged powders were ground in a mortar, suspended in ethanol, and dropped on a 100 × 400 mesh carbon coated Cu grid (Quantifoil Micro Tools GmbH) on which Au colloidal particles (6.5 nm for the fresh and 10 nm for aged powders) were deposited before. The scanning transmission electron microscopy (STEM) measurements were performed using an image corrected Titan 80 300 TEM (FEI Company) operated at an acceleration voltage of 300 kV in the Karlsruhe Nano Micro Facility (KNMF). STEM images were collected with a high angle annular darkfield (HAADF) detector over a tilt range of −72° to +70° for the fresh powder and from −74° to +76° for the aged powder with 2° increments. Alignment of the tilt series was performed in IMOD using the Au colloidal particles as fiducial markers with a mean residual alignment error of 0.727 pixels and 0.451 pixels for the fresh and aged sample, respectively. The aligned tilt series were further reconstructed using the simultaneous iterative reconstruction technique (SIRT) and discrete algebraic reconstruction technique (DART) implementation of the TomoJ plugin[26] in Fiji to obtain segmented reconstructions, which were visualized in Amira (FEI Company) and for pore structure analysis.

RESULTS AND DISCUSSION

The material, which is synthesized by the thermal hydrolysis of CAN, is characterized by spherical micrometer sized particles as seen Figure 1. These spheres with a size between 1 and 4 μm (cf. Figure S1) exhibit a substructure like a cauliflower in both fresh and aged powders.

The micrometer sized structure is not changed during aging. The nanometer sized subunits possess a mean size of 27 nm after the aging as hinted in Figure 1f (cf. Figure S2 for the size distribution of the mesoporous subunits). Interestingly, SEM analysis can reveal substantial remaining mesoporosity after aging (Figure 1f), which is corroborated by the in depth physisorption analysis (see below). Structural changes induced by the aging occur on the nanometer scale, as revealed by TEM analysis (Figure 2), showing that the spherical primary particles start to develop faceting during aging. Simultaneously, the primary particles grew from 4 to 20 nm (cf. Figure S3), which corresponds well to the crystallite dimensions calculated from XRD data by the Scherrer equation (Table 1).

The coincidence of the TEM and XRD based particle dimensions indicates that the primary particles are each single crystalline and agglomerate to the 10 nm species, which are observed in our previous SAXS study.[15] These characteristics of the primary particles evidenced by electron microscopy suggest that significant structural changes occur at the level of nanoparticles, certainly affecting their mutual connection. Nevertheless, while the pore space is altered, it is not destroyed upon aging. This will be further discussed on the basis of advanced physisorption, SAXS analysis and electron micros copy based tomography analysis described below.

Electron microscopy already suggests high crystallinity, which is supported by the XRD patterns (Figure 3) showing all the reflections of cubic cerium oxide (reference code: ICOD 01 081 0792). Furthermore, the lattice constants a of the fresh and aged powders are equal to that of the bulk ceria (CeO_2: 5.410 Å) (Table 1) indicating a negligible amount of oxygen vacancies

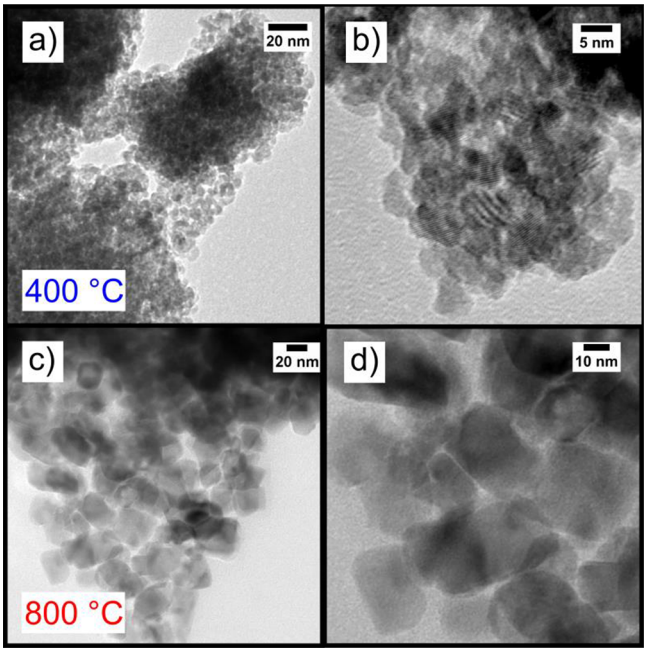

Figure 2. TEM images of the powders after calcination at 400 °C (a, b) and after aging at 800 °C (c, d).

Table 1. Crystallite Size $L_{Scherrer}$ Obtained by the Scherrer Equation from XRD Data, Particle Size L_{TEM}, and Particle Morphologies Obtained from TEM Images of the Primary Particles and the Lattice Constant *a* of the Fresh (400 °C) and Aged (800 °C) Samples

temperature	$L_{Scherrer}$/nm	L_{TEM}/nm	particle morphology	*a*/Å
400 °C	4	4	spherical	5.410
800 °C	20	20	edged	5.405

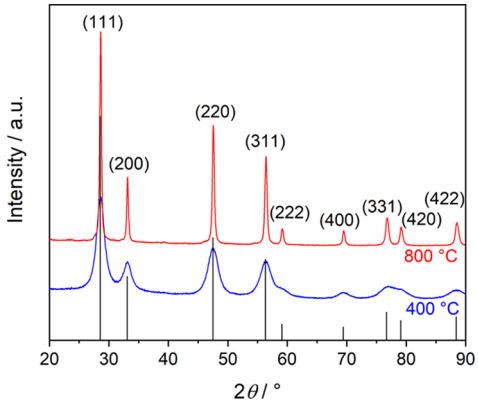

Figure 3. XRD patterns of the powders after calcination at 400 °C and after aging at 800 °C and reference reflections.

and Ce^{3+} in the bulk. If an increased amount of Ce^{3+} ions (possessing a higher ionic radius of 1.034 Å compared to 0.92 Å of Ce^{4+} ions) was present in the samples, the material would exhibit a higher lattice constant.[27] Hence, almost stoichiometric $CeO_{2.0}$ has already been formed during the synthesis, which remains unchanged during aging. The negligible amount of bulk defects is also proven by small Raman signals within the so called defect band region between 550 and 650 cm^{-1} (Figure 4).[28] Additionally, the intensity ratio of the defect induced D mode (at approximately 594 cm^{-1}) and the characteristic F_{2g} signal

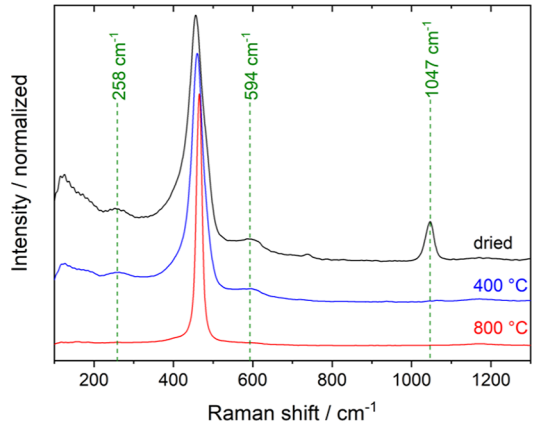

Figure 4. Raman spectra of the powders after drying at 80 °C, calcination at 400 °C, and aging at 800 °C.

(described below) represents the relative defect concentration, which is low for all three samples (≤0.12), as illustrated in Figure S4. If oxygen vacancies are accumulated at the surface, the intensity of the Raman mode at 250 cm^{-1} is reduced, which arises from the longitudinal Ce−O stretching in the topmost layer of the (111) surface.[29] Such low intensity of this surface mode is indeed observed for the investigated fresh and aged powders, while the aging at 800 °C results in the absence of the mode due to a larger number of surface defects. Moreover, all samples generate the characteristic F_{2g} mode associated with the symmetrical stretching mode of oxygen ions around each cation. It is blue shifted upon thermal treatment of the powder at elevated temperatures from 460 cm^{-1} of the fresh powder to 466 cm^{-1} of the aged powder (corresponding to a shift of 6 cm^{-1}) along with increasing particle size from 4 to 20 nm (Figure S4). Similarly, Spanier et al. showed a F_{2g} shift of 5 cm^{-1} for nanoparticles of the same size (i.e., 6 and 21 nm).[30] As they observed simultaneously a lattice expansion upon decreasing particle size, they assumed that the F_{2g} shift can be rationalized by reduction effects. In the present work, however, this assumption can be excluded as almost no bulk defects are observed. The observed shift of the Raman mode can, thus, be attributed solely to size effects, which we have already shown for CeO_2 single nanoparticles with different sizes but also fewer defects in the bulk.[31] Finally, a mode is seen at 1047 cm^{-1} in the Raman spectrum of the dried powder, which is caused by the symmetrical stretching of nitrates.[32] After calcination at 400 °C, this mode disappears upon decomposition of the nitrogen oxide species. As seen by TG MS analysis (Figure 5a), the MS signal for NO (m/z = 30) originating from nitrate/nitrite attached to the surface disappears beyond 580 °C, i.e., nitrogen oxide moieties are removed from the particles, starting from ∼280 °C. In order to relate the temperature induced structural changes, especially of the particle size and the mesoporosity, to these chemical alterations, the following set of experiments was performed: Based on the TG MS results, the dried powder was heated to different temperatures between 280 and 630 °C (in steps of 50 °C) at which the MS signals for NO (m/z = 30) and NO_2 (m/z = 46) point to the decomposition of these species. After reaching the target temperature, the respective sample was directly extracted from the oven, i.e., without holding at this temperature, and subjected to investigation by elemental analysis, XRD, and physisorption. The elemental analysis revealed the presence of 2 wt % nitrogen after drying the solid at 80 °C (Figure 5b). The nitrogen amount decreases with

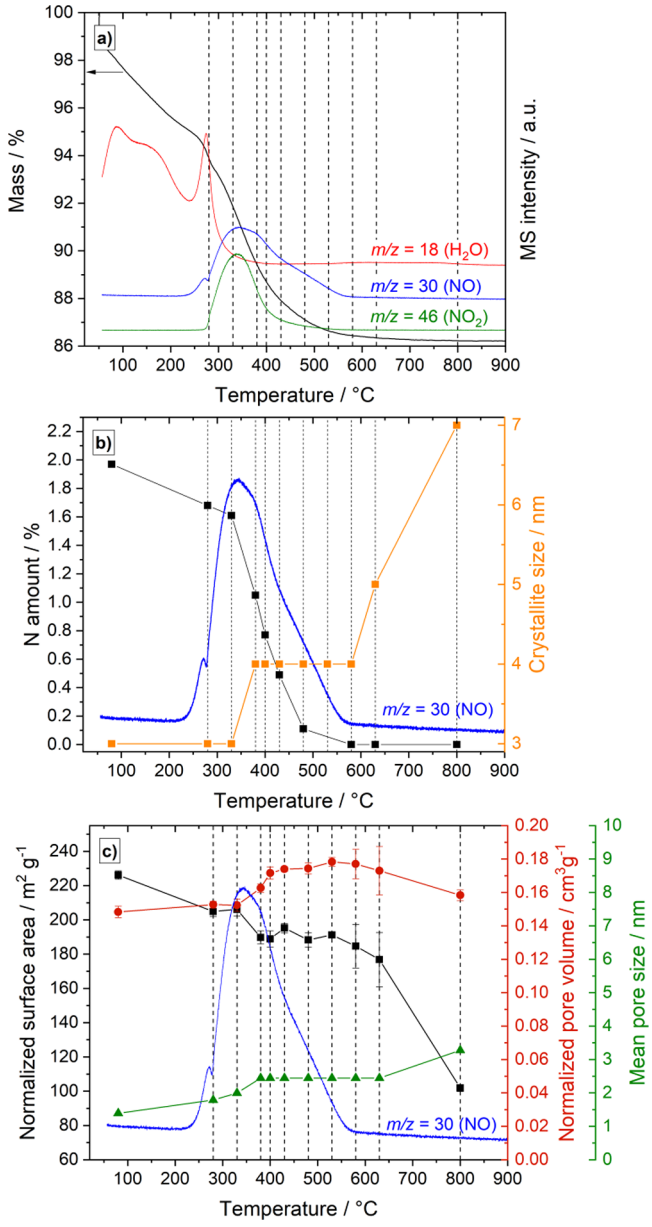

Figure 5. (a) TG MS analysis of the dried powder. Dashed lines indicate the temperatures to which the dried powder is heated up. (b) Elemental analysis on the nitrogen amount and crystallite sizes calculated from the XRD data. (c) Normalized physisorption results for the powders dried at 80 °C and heated up to different temperatures ranging between 280 and 800 °C.

increasing temperature in accordance with the MS signal for NO ($m/z = 30$), which shows a maximum NO release at around 345 °C, while NO is released up to a quite elevated temperature of ~550 °C (Figure 5b). Hence, in the temperature range between 330 and 380 °C, the material exhibits structural alterations associated with the removal of nitrogen oxide species: the crystallite sizes calculated from the respective XRD patterns (cf. Figure S5) increased slightly from 3 to 4 nm, which is significant as the corresponding XRD patterns themselves significantly differ from each other in the width of the reflections (cf. Figure S6). Also, the overall pore volume increases slightly from 0.15 to 0.16 $cm^3\ g^{-1}$ coupled with a decrease in the surface area of the material from 205 to 190 $m^2\ g^{-1}$ (Figure 5c). The explanation for that might be the differences in the obtained pore size distribution for the samples heated to 330 and 380 °C, which is shifted to bigger pores at 380 °C (cf. Figure S7). Notice that these physisorption results were confirmed by repeating the measurements of each sample three times, and averaged values for the respective parameters are provided here. Additionally, the data are normalized to the actual mass of cerium oxide by excluding the nitrogen oxide content of the samples especially at lower temperatures. In consequence, the desorption of the nitrogen oxide species leaves dangling bonds on the surface of the particles and evokes the growth of the crystallites, which rearrange in the secondary structure. The apparent disagreement between the temperature range of NO_x removal and the onset of crystallite growth can be explained by the continuous temperature increase in the TG MS experiment: since crystal growth, requiring the rearrangement of atoms, occurs more slowly than the removal of surface species, the applied heating ramp (5 K min^{-1}) results in an offset between these two parameters. The observation that the mesopore volume stays approximately constant, while the surface area decreases significantly and the mesopore size distribution shifts to slightly larger diameters, points to a closure of small mesopores and micropores. The noticed changes in this experiment, however, are probably less pronounced compared to the actual temperature treatment program used in the synthesis protocol because the samples are not held at the respective temperature but taken out of the oven as soon as the respective temperature was reached. In conclusion, the combined experiments shown in Figure 5 suggest that the nitrogen oxide species act as stabilizing agents against particle sintering and growth, and their removal allows for particle fusion and hence sintering, which thereby strongly affects the nanoscale structure. Thus, structural changes in particle size and mesoporosity occur during their removal at temperatures in the range of 350–500 °C: the dangling bonds at the surface, generated by nitrogen oxide removal at the elevated temperature, possibly allow for a surface diffusion process, resulting in the connection of surfaces of adjacent particles, which in turn closes micropores and small mesopores, thus explaining the accompanying changes in the porosity. Raising the temperature further above 600 °C causes sintering so that the particles grow to 7 nm and the surface area drops to 100 $m^2\ g^{-1}$ at 800 °C. Here again, the crystallite size of 7 nm observed at 800 °C is smaller than the 20 nm crystallites in the aged powder, which was treated for an elongated time (16 h) at the same temperature (800 °C). The impact of the thermal treatment on the nanoscale was further investigated by nitrogen physisorption measurements. The BET analysis on the nitrogen physisorption isotherms in Figure 6 reveals a high surface area of 195 $m^2\ g^{-1}$ for the fresh powder, which drops to 24 $m^2\ g^{-1}$ after aging at 800 °C for 16 h. The fresh material consists of pores ranging from 2 to 8 nm (Figure 6c) whereby the mean pore size is thus of the same dimension as the crystallites (4 nm in size), indicating a defined pore structure and, hence, a controlled assembly of the primary particles. In contrast to this, if the particles (synthesized by, e.g., the precipitation method) are randomly oriented and clump together during the calcination, the pore size distribution would be broader (cf. Figure S8). Consequently, during the thermal hydrolysis the agglomeration of the primary particles into the secondary structure occurs in a controlled manner in the way that these nanobuilding blocks form preliminary stages of agglomerates with nanometer sizes during the hydrolysis at lower temperatures (i.e., below 100 °C), as we proposed in our previous work.[15]

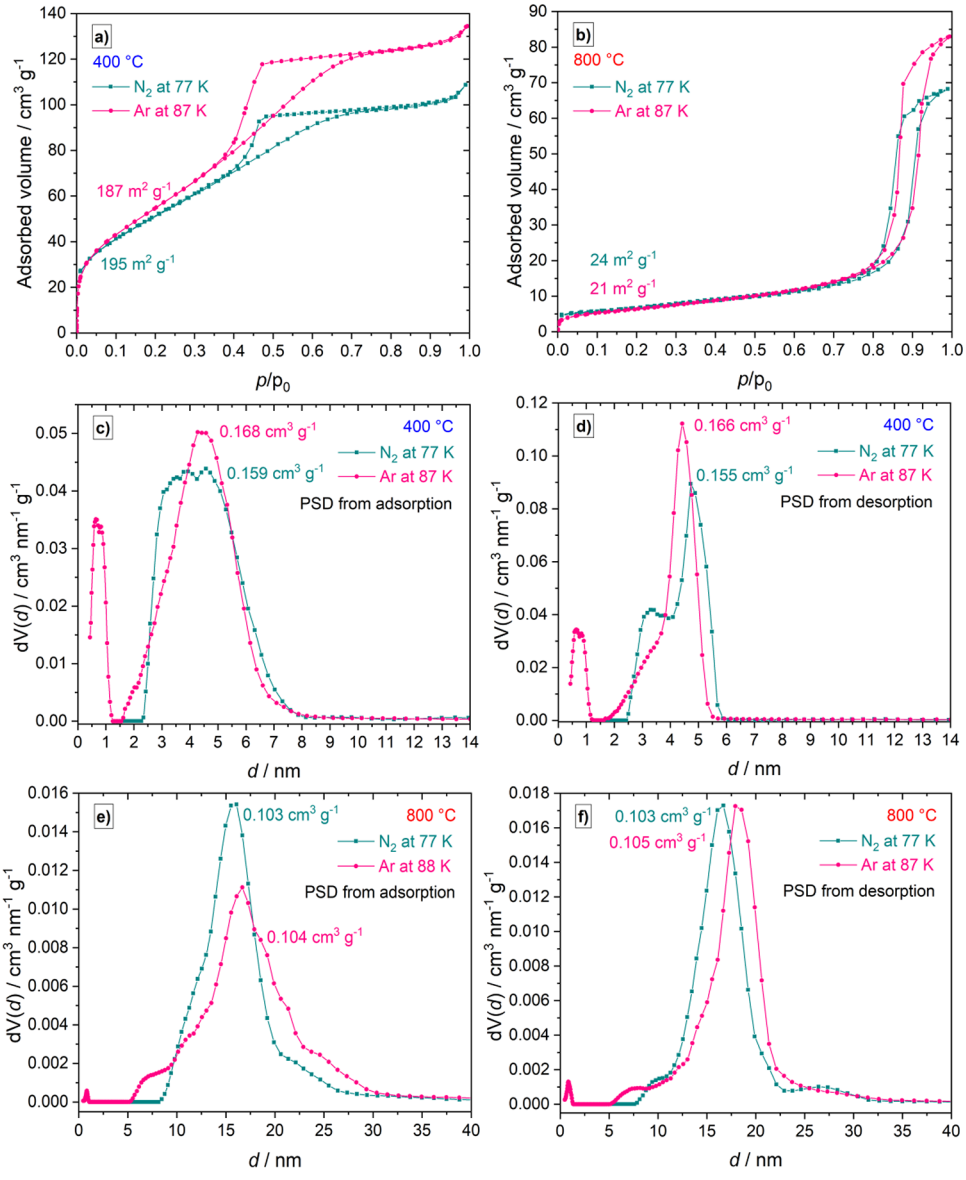

Figure 6. N_2 (77 K) and Ar (87 K) physisorption isotherms of (a) fresh (400 °C) and (b) aged (800 °C) samples as well as the pore size distributions calculated from the adsorption and desorption branches of the fresh (c, d) and aged (e, f) samples, using the NLDFT method (cylindrical pores).

The thermal treatment of the powder at 800 °C causes a broadening of the pore size distribution and a shift toward bigger pores with sizes between 8 and 26 nm (Figure 6e). Also, the shape of the hysteresis curves changes: the fresh powder has a hysteresis loop classified as Type H2 according to IUPAC, which points to a complex pore system such as pore networks with ink bottle shaped pores.[33] By contrast, the physisorption data of the aged powder correspond to a type H1 isotherm, which is often associated with porous materials consisting of independent pores.[33] In order to fully characterize the pore structure, a comprehensive understanding of the observed hysteresis loops is needed. The shape of the hysteresis loop is determined by the adsorption and desorption mechanism, the latter being correlated to the mesopore connectivity. A powerful technique for the differentiation between equilibrium desorp tion, pore blocking, and cavitation is the use of different adsorptives in the physisorption experiments.[34] In Figure 6, the results of the nitrogen (77 K) physisorption measurements are contrasted with the argon (87 K) measurements for the fresh and aged samples. The total pore volume at $p/p_0 = 0.95$ of the fresh sample (400 °C) determined by Ar (87 K) is ~130 $cm^3 g^{-1}$ and, thus, higher than the value of 100 $cm^3 g^{-1}$ measured by N_2 (77 K), which lies within the difference expected for these two fluids. A similar difference in the total adsorbed volume applies also for the aged powder (Ar: 80 $cm^3 g^{-1}$ and N_2: 65 $cm^3 g^{-1}$). The comparison of the pore size distributions (PSD) obtained from two different adsorptives was shown to provide invaluable insight into the connection of mesopores and to differentiate between pore emptying mechanisms (pore blocking vs cavitation).[34] The PSD calculated from the adsorption branches of nitrogen and argon isotherms of the fresh powder (Figure 6c), using the NLDFT method, are almost identical, exhibiting a maximum value at around 5 nm, while a substantial portion of larger mesopores is revealed in this PSD. The PSDs determined from the desorption branches of the nitrogen and argon isotherms (Figure 6d) possess a maximum value at ~5 nm and differ slightly by a shift of ~0.5 nm, which lies within the uncertainty range of the analysis. However, this PSD is markedly

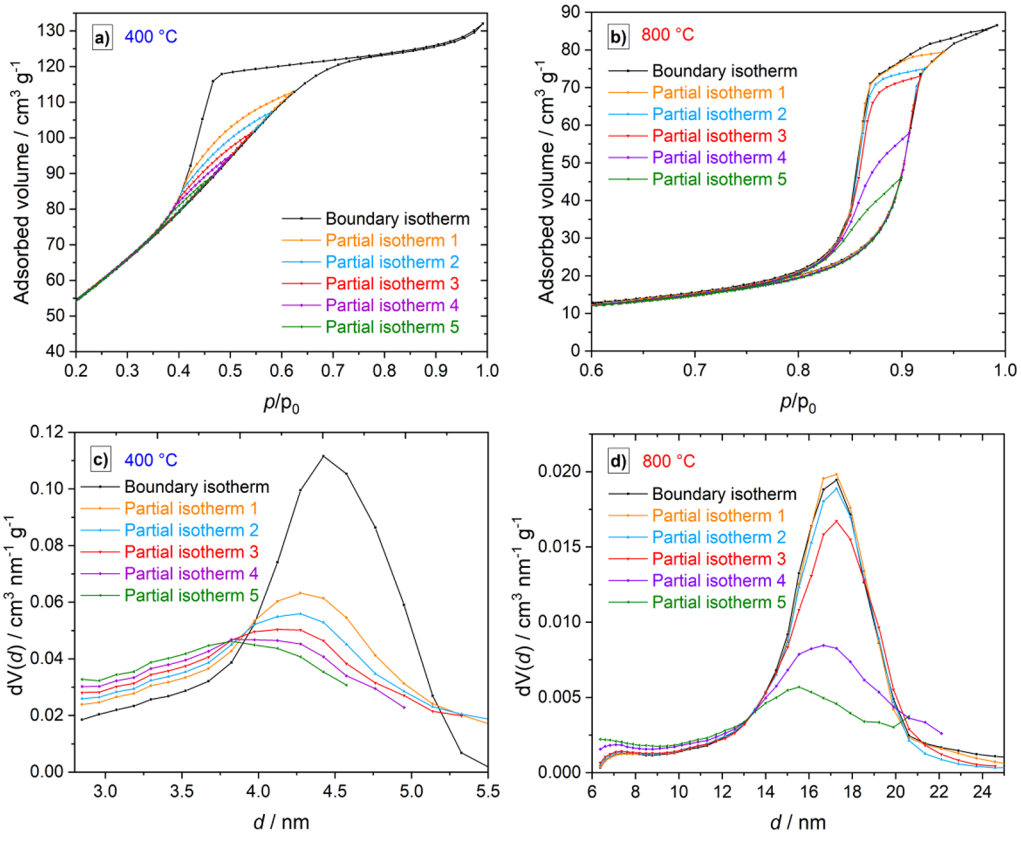

Figure 7. (a, b) Desorption scanning isotherms (Argon at 87 K) and (c, d) resulting pore size distributions of the fresh (400 °C) and aged (800 °C) samples.

sharper than the one extracted from the adsorption branch. Thus, the evaporation pressure for the largest mesopores is controlled by the neck size and not by the adsorptive (i.e. N_2 or Ar), indicating pore blocking effects in pore networks for the fresh powder.[34] The narrow maximum at 5 nm in the PSDs obtained from the desorption branches corresponds to the size of the geometrical neck size, which is seen in the isotherms as a kink in the desorption branch. The PSDs (adsorption/desorption) of the aged material are broader for both adsorptives, and the average mesopore size is larger (~15 nm). Yet, for this sample, the difference between the argon and nitrogen based PSDs (desorption) is more pronounced in that the maximum of the PSDs is shifted by 2 nm, which is more significant compared to the fresh sample (Figure 6f). According to the literature, this discrepancy observed by using two different adsorptives is an indication for cavitation induced evaporation from the pores, which is controlled by the size of the pore necks. This phenomenon occurs if mesopores of 6 nm and larger are connected through significantly smaller meso or micro pores.[34,35] Applying this concept to the present study means that the aging process causes the growth of the mesopores and simultaneously the connecting necks of the mesopores get thinner, i.e., below the critical size, which is responsible for the cavitation in the bigger pores. In order to elucidate the mesopore connectivity in further detail, desorption scanning isotherms using argon physisorption were measured for the fresh and aged powders (Figure 7).[17,18,36] The partial isotherms of the fresh powder (calcined at 400 °C) differ from the shape of the boundary isotherm in that they are not parallel to it. Hence, from the shape of the scanning isotherms, two types of mesopore connectivity can be excluded for this sample, namely, independent mesopores (such as in MCM 41) and ink bottle mesopores being connected through micropores or small mesopores, resulting in cavitation. This interpretation of the hysteresis scanning curves is in accordance with the analysis of the entire isotherms, described in Figure 6. The most striking feature of the fresh powder is, thus, the marked difference between the shapes of the overall isotherm and the scanning isotherms (Figure 7a). This deviation implies that the larger mesopores are connected and therefore empty differently compared to the smaller mesopores. In general, the reason for such behavior is the dependence of the evaporation from the state of the neighboring pores. Consequently, the mesopores are interconnected with each other and build an extended pore network in which the evaporation occurs after the confined liquid evaporates from the largest neck (pore blocking effect) as already shown by the comparison of the argon and nitrogen physisorption results.[17] The mesopore space of the aged powder is different from the fresh sample, as seen in the corresponding scanning isotherms (Figure 7b). Although the initial hysteresis curve was assigned to a type H1 hysteresis by the nitrogen physisorption results in Figure 6b, the desorption scans have a more complicated evolution (Figure 7b). The H1 hysteresis type is usually formed by independent pores, and in this case the shape of the desorption scans should be similar to the boundary isotherm.[36] While the first three partial isotherms (in orange, light blue, and red) of the aged powder resemble the boundary isotherm, the curves at lower pressures (partial isotherms 5 and 6 in violet and green) have a different shape. This observation suggests the coexistence of two types of mesopores of approximately similar concentration in the aged sample: mesopores that are connected through small necks (in the

sense of cavitation) and independent pores that feature unhindered adsorption/desorption. Their sizes, however, cannot be differentiated as the PSDS of all segments in Figure 7d are within the same pore size range. Based on these physisorption scanning experiments, we conclude that the aging process causes a partial change of the pore structure, in particular, the mesopore connection (Scheme 2). Starting from

Scheme 2. Illustration of the Mesopores (in Gray) in the (a) Fresh (400 °C) and (b) Aged (800 °C) powders[a]

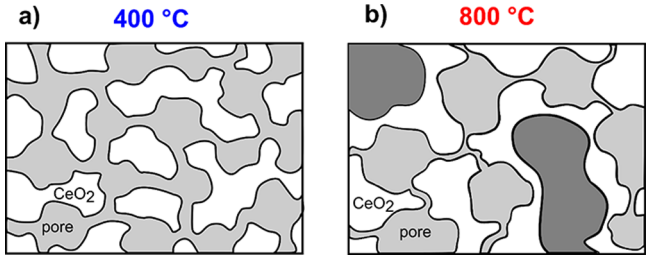

[a]The two mesopore types in the aged powder are depicted in two different gray shades: interconnected pores in light gray and isolated pores in dark gray.

a pore network in the fresh powder in which the pores are interconnected by small necks, sintering leads to a decrease in the neck size in the aged sample so that the evaporation from the pores cannot take place by emptying of these necks but by formation of bubbles in the condensed fluid within the mesopores (cavitation mechanism). To some extent, these connecting units disappear partially upon treatment at 800 °C while the bigger pores grow, a process similar to Ostwald ripening of nanomaterials. As indicated by the TG MS experiments, these processes start already at lower temperatures in the range of 400 to 600 °C. As a consequence, independent pores (dark grey in Scheme 2) and a pore network connected by small necks coexist in the aged powder.

More detailed information with respect to the porosity can be obtained by electron tomography analysis, which provides insights into the particle's interior at the nanoscale. For that reason, the 3D morphology of the fresh and aged powders was analyzed by the physical reconstruction of the pore space (Figure 8) based on tilt series of 2D projection images acquired

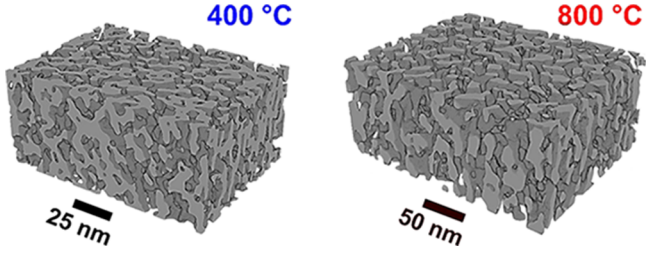

Figure 8. 3D reconstruction of the fresh (400 °C) and aged (800 °C) powders by nanoscale tomography.

using scanning transmission electron microscopy (STEM, cf. Figure S9). The block views of parts of the reconstructed and segmented micrometer sized spherical particles in Figure 8 reveal the morphological changes at the nanoscale very well. In both samples, the material is highly porous, but after the aging, the CeO_2 network gets thicker as already observed in the microscopy analysis in Figures 1 and 2. In order to gain deeper insights into the particles' interior, slices through the reconstructed particles are depicted in Figure 9. For a better

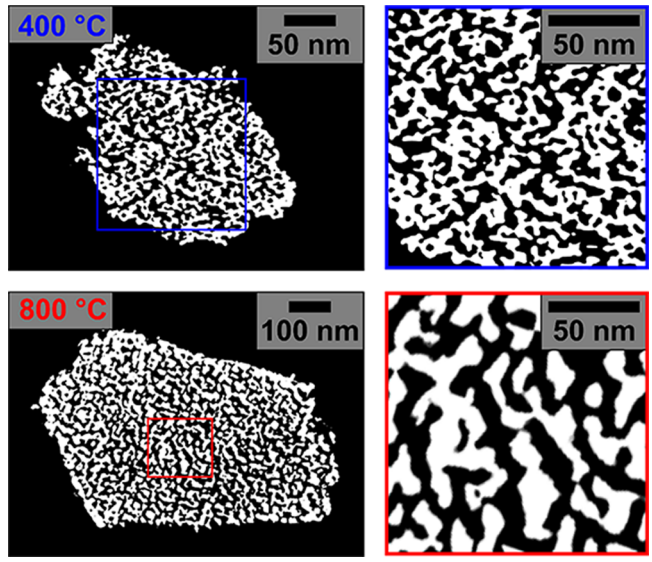

Figure 9. Slices through the 3D reconstructions of the fresh (400 °C) and aged (800 °C) samples. CeO_2 in white and pores in black.

comparison of both investigated samples, the marked sections are expanded to the same magnitude. All of these results show the continuous connectivity of the pores in the mesopore space with a mean pore coordination number of three of the fresh powder (cf. Figure S10). Accordingly, a continuous 3D network of crystalline CeO_2 is present in the fresh powder, which is in in good accordance to the physisorption results. This network structure is still present after aging but coarser as seen in the broader walls and larger pores in the reconstructions, and the mean pore coordination number here is also three (cf. Figure S10). For a qualitative description of these observations, a skeletonization function was applied on the reconstructions in order to extract information about the topological properties of the investigated materials, like the wall thickness, pore sizes, and the already mentioned mean pore coordination numbers. For the fresh powder, the pore size distribution obtained from the 3D reconstruction by the skeletonization function is in good agreement with the number weighted pore size distribution obtained by NLDFT analysis on N_2 physisorption results with pore sizes ranging from 2 to 8 nm (Figure 10a). On the contrary, slight differences are present especially at smaller pore sizes of the aged powder as the physisorption results show the presence of pores between 8 and 26 nm (Figure 10b). These smaller pores (voids) are not detected by physisorption. In general, however, the physisorption results are confirmed by the reconstruction data and the mesopores grow on the average during the aging at 800 °C, but the 3D mesopore structure is preserved in both cases as the coordination number is identical (cf. Figure S10).

The thickness of the ceria walls (solid) in the mesopore space of the fresh powder ranges from 2 to 7 nm, which corresponds well to the crystallite size of 4 nm obtained from the XRD data (Figure 11a) and confirms that the 10 nm agglomerates observed in the in situ SAXS analysis are an assembly of the primary particles.[15] The aforementioned dimensions of the mesopores, the walls, and the primary particles indicate that the wall thickness rather equals the size of a single primary particle and not the agglomerate size of 10 nm. This means that the

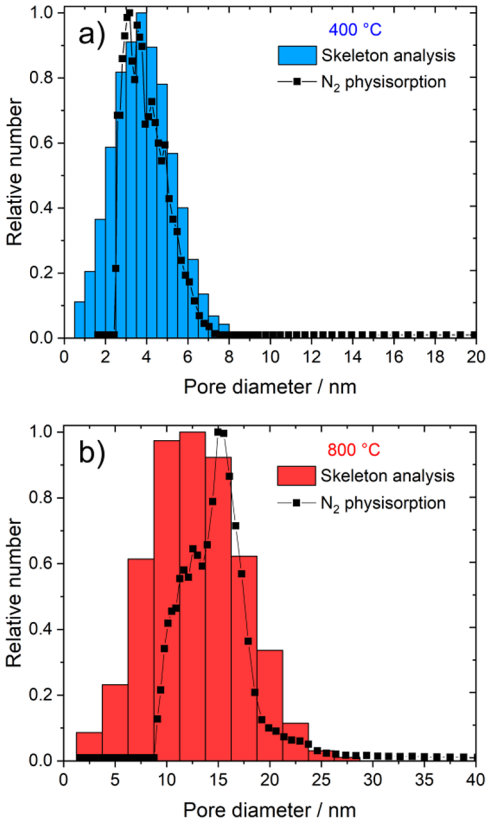

Figure 10. Pore size distributions of the (a) fresh (400 °C) and (b) aged (800 °C) powders obtained from the 3D reconstruction in comparison to the number weighted pore size distributions obtained by N_2 physisorption.

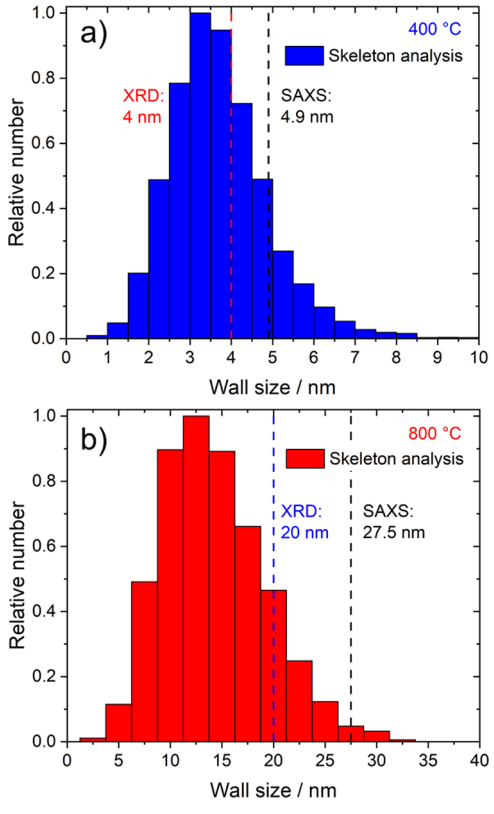

Figure 11. Wall size distributions of the (a) fresh (400 °C) and (b) aged (800 °C) powders obtained from the 3D reconstruction in comparison to the crystallite sizes calculated from XRD data and the mean wall thicknesses obtained from the SAXS analysis.

primary particles form a linear chain, the width corresponding to the mesopore wall thickness and not to the agglomerate size of 10 nm. However, it is challenging to obtain further evidence for this structural model, as it is difficult to prove the state of the agglomerates during the formation of the secondary structure. The thermal treatment at 800 °C causes the growth of these walls possessing a mean size of 20 nm, which again matches the domain size calculated by the Scherrer equation (Figure 11b).

Finally, SAXS was applied for elucidating the mesoporosity in this disordered pore system. Significant differences were obtained between the two corresponding SAXS patterns of the fresh and aged samples (Figure 12a). After aging, the SAXS curve follows the Porod's law almost ideally, i.e., the intensity is proportional to s^{-4} over a large range of the modulus of the scattering vector s. Both curves do not display any distinct features indicating a random mesopore structure as also seen in the nanoscale tomography. The SAXS data are further evaluated by the concept of chord length distribution (CLD), which is basically a statistical distribution of surface to surface distances in a two phase system consisting of solid and void.[37] Figure 12b shows the plot of the CLDs of the fresh and aged powders. As the CLD is a superposition of the chord length of the void space and the pore walls, the maxima and minima in the distributions do not reveal directly the corresponding wall or pore size.

Additional information is obtained from the CLD's first moment, which is the so called Porod length l_p. It can be used to calculate the average void (pore) size l_v and wall thickness l_w without assuming a predefined morphology like in the evaluation of the physisorption data (eq 1).[37]

$$\frac{1}{l_p} = \frac{1}{l_w} + \frac{1}{l_v} = \frac{1}{\phi \cdot l_w} = \frac{1}{(1-\phi)\cdot l_v} \quad (1)$$

Thereby, Φ is the volume fraction of the pores, which is obtained from physisorption data because absolute SAXS intensities were not accessible. The results of this evaluation (Table 2) concur well with previous results obtained from XRD and physisorption analysis as well as the mean values obtained from the results of the nanoscale tomography.

It also possible to apply the CLD analysis on the reconstruction data, which we conducted on both fresh and aged powders (Figure S12 and Table S1). The resulting pore sizes and wall sizes, however, differ from the results by XRD, physisorption, and CLD analysis from SAXS data. Such discrepancy was already observed in our previous study of silica monoliths but has not been resolved yet.[38] Consequently, the CLD analysis on reconstructed data has to be further improved, which will be the topic of further investigations.

CONCLUSIONS

In this study, the temperature induced changes in the disordered mesopore space of a porous CeO_2 material were studied by the combination of state of the art analysis, comprising in depth physisorption studies, electron tomography, SAXS, and TG MS. The synthesis via thermal hydrolysis of CAN at 150 °C provides a CeO_2 nanomaterial with a high surface area and porosity. Its morphology is characterized by the self assembly of the primary particles to micrometer sized spheres.

Our TG MS studies suggest that the stability of the mesopore space is related to the chemical moieties bound to the particles'

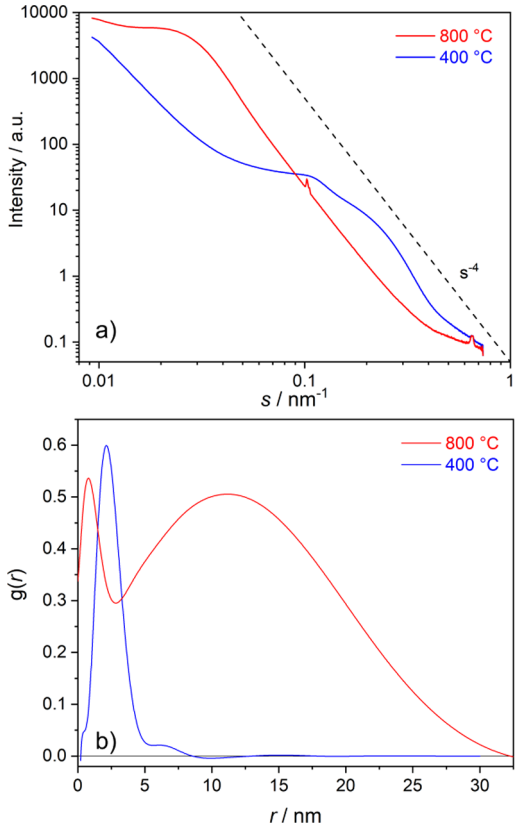

Figure 12. (a) SAXS curves and (b) calculated chord length distribution $g(r)$ of the fresh (400 °C) and aged (800 °C) powders.

Table 2. Summary of the Results for the Mean Pore Size and Mean Wall Size Obtained by SAXS (CLD) Analysis from Data (using eq 1), XRD (Scherrer Equation), Physisorption (N_2, Adsorption, Mode), and Electron Tomography (Skeleton Analysis Mode)

temperature		SAXS	XRD	physisorption	skeleton analysis
400 °C	pore size	5.5 nm		4.5 nm	3.5 nm
	wall size	4.9 nm	4.0 nm		3.2 nm
800 °C	pore size	11.9 nm		16 nm	12.8 nm
	wall size	27.5 nm	20 nm		14.3 nm

surface: It is shown that the presence and the removal of remaining nitrogen oxide species are related to structural properties of the nanomaterial on the nanoscale. Upon their removal at temperatures above 300 °C, the primary particles grow and undergo structural rearrangement, resulting in alterations of the mesopore space. Yet, the micrometer sized secondary structure is preserved. The details of these morphological characteristics are visualized and quantified by electron tomography, which reveals the 3D mesopore network structure. Additionally, the mesoporosity is further examined by hysteresis scanning experiments, which confirmed the presence of a network of mesopores in the fresh powder. During the sintering, the connecting necks get thinner and vanish to some extent. Therefore, two types of pores are present in the aged powder: while some of them remain still in a network structure, others are separated from them and, thus, exist as single pores. Finally, the results are then compared to the SAXS analysis, which is especially suitable to investigate disordered meso porous nanomaterials and thus delivers complementary information to the physisorption results. The structural parameters obtained from different methods, in particular, the mesopore size and the wall thickness, agree reasonably, confirming the underlying assumption, especially in the case of the physisorption analysis. More importantly, electron tomog raphy supports the detailed physisorption scanning isotherm analysis and the conclusion drawn therefrom. Since the interpretation of scanning isotherm data are still a matter of intense debate, this study, thus, might help to provide guidelines for further advancement of this method.[39]

Our study therefore complements mechanistic investigations on the solution based synthesis of these nanoparticles (Scheme 3).[15] In that recent study, we used SAXS to elucidate the nucleation and growth process of these particles, in particular, the particle size distribution and agglomeration. It was found that small nanoparticles form on the order of 2 nm in diameter, which partially assemble into agglomerates of ~10 nm already at room temperature. Based on this previous and the current study, it is now possible to propose a coherent view on the mesopore structure and its formation, starting from the colloidal dispersion over the self assembly of the particles/agglomerates and the 3D mesopore framework: The CeO_2 walls consisting of single crystallites are connected to each other in a loose 3D structure, whereby the pores possess a similar size as the walls form an open network and are responsible for the high surface area of this material. The controlled assembly of the primary particles is enabled by their agglomeration into nanometer sized agglom erates at hydrolysis temperatures up to 100 °C, as we had found in a previous study. We propose here that these pre agglomerates form a structure similar to a pearl necklace within the secondary structure (Scheme 3), which is manifested at the

Scheme 3. Summary of the Results in Combination with the Results for the Thermal Hydrolysis at Temperatures below 100 °C Presented in Our Previous Publication[15]

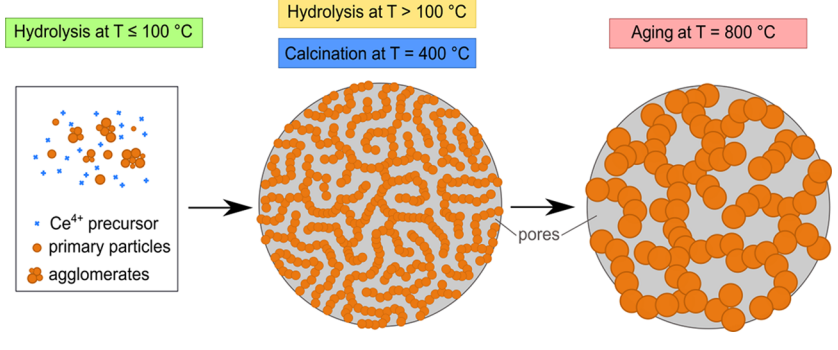

early stages of the synthesis. Hence, a highly porous and crystalline material comparable to a coral is obtained in which the crystallites are connected to each other in an energetically favorable fashion and do not underlie too pronounced sintering, because of the 1D character of their mutual connection. Only upon harsh conditions during the aging (800 °C), substantial structural rearrangement occurs, while the material still possesses a quite high mesopore volume. In conclusion, this study now provides an experimental basis for further studies on the formation mechanism of 3D mesopore frameworks as well as the validation of characterization techniques, especially physisorption.

AUTHOR INFORMATION

Corresponding Author

Bernd M. Smarsly − *Institute of Physical Chemistry, Justus Liebig University, 35392 Giessen, Germany; Center for Materials Research (LaMa), Justus Liebig University, 35392 Giessen, Germany;* orcid.org/0000 0001 8452 2663; Email: bernd.smarsly@phys.chemie.uni giessen.de

Authors

Elifkübra Özkan − *Institute of Physical Chemistry, Justus Liebig University, 35392 Giessen, Germany; Umicore AG & Co. KG, 63457 Hanau, Germany*

Alexander Hofmann − *Umicore AG & Co. KG, 63457 Hanau, Germany;* orcid.org/0000 0001 9872 2156

Martin Votsmeier − *Umicore AG & Co. KG, 63457 Hanau, Germany; Department of Chemistry, Technical University Darmstadt, 64287 Darmstadt, Germany;* orcid.org/0000 0002 3842 7136

Wu Wang − *Institute of Nanotechnology, Karlsruhe Institute of Technology, 76344 Eggenstein Leopoldshafen, Germany*

Xiaohui Huang − *Institute of Nanotechnology, Karlsruhe Institute of Technology, 76344 Eggenstein Leopoldshafen, Germany; Department of Materials and Earth Science, Technical University Darmstadt, 64287 Darmstadt, Germany*

Christian Kübel − *Institute of Nanotechnology, Karlsruhe Institute of Technology, 76344 Eggenstein Leopoldshafen, Germany; Department of Materials and Earth Science, Technical University Darmstadt, 64287 Darmstadt, Germany;* orcid.org/0000 0001 5701 4006

Felix Badaczewski − *Institute of Physical Chemistry, Justus Liebig University, 35392 Giessen, Germany; Center for Materials Research (LaMa), Justus Liebig University, 35392 Giessen, Germany*

Kevin Turke − *Institute of Physical Chemistry, Justus Liebig University, 35392 Giessen, Germany*

Sebastian Werner − *Institute of Physical Chemistry, Justus Liebig University, 35392 Giessen, Germany*

Author Contributions

The manuscript was written through contributions of all authors. All authors have given approval to the final version of the manuscript.

Notes

The authors declare no competing financial interest.

ACKNOWLEDGMENTS

Financial support is provided by the Research Training Group (RTG) 2204 of the German Research Foundation (DFG) and Umicore AG & Co. KG. We would like to thank Robert Greiner and Eric Prates da Costa for their assistance in creating the figures showing the tomography results.

REFERENCES

(1) Trovarelli, A. Catalytic Properties of Ceria and CeO_2 Containing Materials. *Catal. Rev.* **1996**, *38*, 439−520.

(2) Trovarelli, A.; de Leitenburg, C.; Boaro, M.; Dolcetti, G. The Utilization of Ceria in Industrial Catalysis. *Catal. Today* **1999**, *50*, 353−367.

(3) Amrute, A. P.; Mondelli, C.; Moser, M.; Novell Leruth, G.; López, N.; Rosenthal, D.; Farra, R.; Schuster, M. E.; Teschner, D.; Schmidt, T.; Perez Ramirez, J. Performance, Structure, and Mechanism of CeO_2 in HCl Oxidation to Cl_2. *J. Catal.* **2012**, *286*, 287−297.

(4) Li, C.; Sun, Y.; Djerdj, I.; Voepel, P.; Sack, C. C.; Weller, T.; Ellinghaus, R.; Sann, J.; Guo, Y.; Smarsly, B. M.; Over, H. Shape Controlled CeO_2 Nanoparticles: Stability and Activity in the Catalyzed HCl Oxidation Reaction. *ACS Catal.* **2017**, *7*, 6453−6463.

(5) Reed, K.; Cormack, A.; Kulkarni, A.; Mayton, M.; Sayle, D.; Klaessig, F.; Stadler, B. Exploring the Properties and Applications of Nanoceria: Is There Still Plenty of Room at the Bottom? *Environ. Sci. Nano* **2014**, *1*, 390−405.

(6) Sun, C.; Li, H.; Chen, L. Nanostructured Ceria Based Materials: Synthesis, Properties, and Applications. *Energy Environ. Sci.* **2012**, *5*, 8475−8505.

(7) Laha, S. C.; Ryoo, R. Synthesis of Thermally Stable Mesoporous Cerium Oxide with Nanocrystalline Frameworks Using Mesoporous Silica Templates. *Chem. Commun.* **2003**, *9*, 2138−2139.

(8) Puertolas, B.; Solsona, B.; Agouram, S.; Murillo, R.; Mastral, A. M.; Aranda, A.; Taylor, S. H.; Garcia, T. The Catalytic Performance of Mesoporous Cerium Oxides Prepared through a Nanocasting Route for the Total Oxidation of Naphthalene. *Appl. Catal. B Environ.* **2010**, *93*, 395−405.

(9) Deshpande, A. S.; Pinna, N.; Smarsly, B.; Antonietti, M.; Niederberger, M. Controlled Assembly of Preformed Ceria Nanocryst als into Highly Ordered 3D Nanostructures. *Small* **2005**, *1*, 313−316.

(10) Corma, A.; Atienzar, P.; García, H.; Chane Ching, J. Y. Hierarchically Mesostructured Doped CeO_2 with Potential for Solar Cell Use. *Nat. Mater.* **2004**, *3*, 394−397.
(11) Mai, H. X.; Sun, L. D.; Zhang, Y. W.; Si, R.; Feng, W.; Zhang, H. P.; Liu, H. C.; Yan, C. H. Shape Selective Synthesis and Oxygen Storage Behavior of Ceria Nanopolyhedra, Nanorods, and Nanocubes. *J. Phys. Chem. B* **2005**, *109*, 24380−24385.
(12) Ohtake, N.; Katoh, M.; Sugiyama, S. High Thermal Stability Ceria Synthesized via Thermal Hydrolysis Route and Methane Combustion Performance. *J. Ceram. Soc. Japan* **2017**, *125*, 57−61.
(13) Hirano, M.; Fukuda, Y.; Iwata, H.; Hotta, Y.; Inagaki, M. Preparation and Spherical Agglomeration of Crystalline Cerium(IV) Oxide Nanoparticles by Thermal Hydrolysis. *J. Am. Ceram. Soc.* **2000**, *83*, 1287−1289.
(14) Li, Y.; Shen, W. Morphology Dependent Nanocatalysts: Rod Shaped Oxides. *Chem. Soc. Rev.* **2014**, *43*, 1543−1574.
(15) Özkan, E.; Badaczewski, F.; Cop, P.; Werner, S.; Hofmann, A.; Votsmeier, M.; Amenitsch, H.; Smarsly, B. M. Peering into the Formation of Cerium Oxide Colloidal Particles in Solution by In Situ Small Angle X Ray Scattering. *Langmuir* **2020**, *36*, 9175−9190.
(16) Cimino, R.; Cychosz, K. A.; Thommes, M.; Neimark, A. V. Experimental and Theoretical Studies of Scanning Adsorption Desorption Isotherms. *Colloids Surf., A* **2013**, *437*, 76−89.
(17) Cychosz, K. A.; Guillet Nicolas, R.; García Martínez, J.; Thommes, M. Recent Advances in the Textural Characterization of Hierarchically Structured Nanoporous Materials. *Chem. Soc. Rev.* **2017**, *46*, 389−414.
(18) Cychosz, K. A.; Guo, X.; Fan, W.; Cimino, R.; Gor, G. Y.; Tsapatsis, M.; Neimark, A. V.; Thommes, M. Characterization of the Pore Structure of Three Dimensionally Ordered Mesoporous Carbons Using High Resolution Gas Sorption. *Langmuir* **2012**, *28*, 12647−12654.
(19) Friedrich, H.; De Jongh, P. E.; Verkleij, A. J.; De Jong, K. P. Electron Tomography for Heterogeneous Catalysts and Related Nanostructured Materials. *Chem. Rev.* **2009**, *109*, 1613−1629.
(20) Midgley, P. A.; Weyland, M. 3D Electron Microscopy in the Physical Sciences: The Development of Z Contrast and EFTEM Tomography. *Ultramicroscopy* **2003**, *96*, 413−431.
(21) Kübel, C.; Voigt, A.; Schoenmakers, R.; Otten, M.; Su, D.; Lee, T. C.; Carlsson, A.; Bradley, J. Recent Advances in Electron Tomography: TEM and HAADF STEM Tomography for Materials Science and Semiconductor Applications. *Microsc. Microanal.* **2005**, *11*, 378−400.
(22) Stoeckel, D.; Kübel, C.; Hormann, K.; Höltzel, A.; Smarsly, B. M.; Tallarek, U. Morphological Analysis of Disordered Macroporous Mesoporous Solids Based on Physical Reconstruction by Nanoscale Tomography. *Langmuir* **2014**, *30*, 9022−9027.
(23) Reich, S. J.; Svidrytski, A.; Hlushkou, D.; Stoeckel, D.; Kübel, C.; Höltzel, A.; Tallarek, U. Hindrance Factor Expression for Diffusion in Random Mesoporous Adsorbents Obtained from Pore Scale Simulations in Physical Reconstructions. *Ind. Eng. Chem. Res.* **2018**, *57*, 3031−3042.
(24) Reich, S. J.; Svidrytski, A.; Höltzel, A.; Florek, J.; Kleitz, F.; Wang, W.; Kübel, C.; Hlushkou, D.; Tallarek, U. Hindered Diffusion in Ordered Mesoporous Silicas: Insights from Pore Scale Simulations in Physical Reconstructions of SBA 15 and KIT 6 Silica. *J. Phys. Chem. C* **2018**, *122*, 12350−12361.
(25) Wang, W.; Svidrytski, A.; Wang, D.; Villa, A.; Hahn, H.; Tallarek, U.; Kübel, C. Quantifying Morphology and Diffusion Properties of Mesoporous Carbon from High Fidelity 3D Reconstructions. *Microsc. Microanal.* **2019**, *25*, 891−902.
(26) MessaoudiI, C.; Boudier, T.; Sorzano, C.; Marco, S. TomoJ: Tomography Software for Three Dimensional Reconstruction in Transmission Electron Microscopy. *BMC Bioinf.* **2007**, *8*, 1−9.
(27) Deshpande, S.; Patil, S.; Kuchibhatla, S. V.; Seal, S. Size Dependency Variation in Lattice Parameter and Valency States in Nanocrystalline Cerium Oxide. *Appl. Phys. Lett.* **2005**, *87*, 133113.
(28) Filtschew, A.; Hofmann, K.; Hess, C. Ceria and Its Defect Structure: New Insights from a Combined Spectroscopic Approach. *J. Phys. Chem. C* **2016**, *120*, 6694−6703.
(29) Schilling, C.; Hofmann, A.; Hess, C.; Ganduglia Pirovano, M. V. Raman Spectra of Polycrystalline CeO_2 : A Density Functional Theory Study. *J. Phys. Chem. C* **2017**, *121*, 20834−20849.
(30) Spanier, J. E.; Robinson, R. D.; Zhang, F.; Chan, S. W.; Herman, I. P. Size Dependent Properties of CeO_{2-y} Nanoparticles as Studied by Raman Scattering. *Phys. Rev. B* **2001**, *64*, 245407.
(31) Özkan, E.; Cop, P.; Benfer, F.; Hofmann, A.; Votsmeier, M.; Guerra, J. M.; Giar, M.; Heiliger, C.; Over, H.; Smarsly, B. M. Rational Synthesis Concept for Cerium Oxide Nanoparticles: On the Impact of Particle Size on the Oxygen Storage Capacity. *J. Phys. Chem. C* **2020**, *124*, 8736−8748.
(32) Filtschew, A.; Stranz, D.; Hess, C. Mechanism of NO_2 storage in Ceria Studied Using Combined in situ Raman/FT IR Spectroscopy. *Phys. Chem. Chem. Phys.* **2013**, *15*, 9066−9069.
(33) Thommes, M.; Kaneko, K.; Neimark, A. V.; Olivier, J. P.; Rodriguez Reinoso, F.; Rouquerol, J.; Sing, K. S. W. Physisorption of Gases, with Special Reference to the Evaluation of Surface Area and Pore Size Distribution (IUPAC Technical Report). *Pure Appl. Chem.* **2015**, *87*, 1051−1069.
(34) Thommes, M.; Smarsly, B.; Groenewolt, M.; Ravikovitch, P. I.; Neimark, A. V. Adsorption Hysteresis of Nitrogen and Argon in Pore Networks and Characterization of Novel Micro and Mesoporous Silicas. *Langmuir* **2006**, *22*, 756−764.
(35) Rasmussen, C. J.; Vishnyakov, A.; Thommes, M.; Smarsly, B. M.; Kleitz, F.; Neimark, A. V. Cavitation in Metastable Liquid Nitrogen Confined to Nanoscale Pores. *Langmuir* **2010**, *26*, 10147−10157.
(36) Thommes, M.; Cychosz, K. A. Physical Adsorption Characterization of Nanoporous Materials: Progress and Challenges. *Adsorption* **2014**, *20*, 233−250.
(37) Smarsly, B.; Groenewolt, M.; Antonietti, M. SAXS Analysis of Mesoporous Model Materials: A Validation of Data Evaluation Techniques to Characterize Pore Size, Shape, Surface Area, and Curvature of the Interface. *Prog. Colloid Polym. Sci.* **2005**, *130*, 105−113.
(38) Stoeckel, D.; Kübel, C.; Loeh, M. O.; Smarsly, B. M.; Tallarek, U. Morphological Analysis of Physically Reconstructed Silica Monoliths with Submicrometer Macropores: Effect of Decreasing Domain Size on Structural Homogeneity. *Langmuir* **2015**, *31*, 7391−7400.
(39) Svidrytski, A.; Hlushkou, D.; Thommes, M.; Monson, P. A.; Tallarek, U. Modeling the Impact of Mesoporous Silica Microstructures on the Adsorption Hysteresis Loop. *J. Phys. Chem. C* **2020**, *124*, 21646−21655.